PHYSICAL REVIEW FLUIDS **10**, 030502 (2025)

Invited Articles    Editors' Suggestion

# Fluid mechanical study of rotation-induced traumatic brain injury

Qifu Wang,[1,2,*] Jiaqi Zhang,[3,4,*] David Bates,[1,2] James J. Feng,[5,6]
Pengtao Yue,[7,†] and Qianhong Wu[1,2,‡]

[1]*Cellular Biomechanics and Sports Science Laboratory, Villanova University, Villanova, Pennsylvania 19085, USA*
[2]*Department of Mechanical Engineering, Villanova University, Villanova, Pennsylvania 19085, USA*
[3]*Research Center for Mathematics, Advanced Institute of Natural Sciences, Beijing Normal University, Zhuhai 519087, China*
[4]*Department of Mathematical Sciences, Faculty of Science and Technology, BNU-HKBU United International College, Zhuhai 519088, China*
[5]*Department of Chemical and Biological Engineering, University of British Columbia, Vancouver, British Columbia V6T 1Z3, Canada*
[6]*Department of Mathematics, University of British Columbia, Vancouver, British Columbia V6T 1Z2, Canada*
[7]*Department of Mathematics, Virginia Tech, Blacksburg, Virginia 24061, USA*

(Received 15 June 2024; accepted 7 February 2025; published 28 March 2025)

Traumatic brain injury (TBI) is a serious health issue. Studies have highlighted the severity of rotation-induced TBI. However, the role of cerebrospinal fluid (CSF) in transmitting the impact from the skull to the soft brain matter remains unclear. Herein, we use experiments and computations to define and probe this role in a simplified setup. A spherical hydrogel ball, serving as a soft brain model, was subjected to controlled rotation within a water bath, emulating the CSF, and filling a transparent cylinder. The cylinder and ball velocities, as well as the ball's deformation over time, were measured. We found that the soft hydrogel ball is very sensitive to decelerating rotational impacts, experiencing significant deformation during the process. A finite-element code is written to simulate the process. The hydrogel ball is modeled as a poroelastic material infused with fluid and its coupling with the suspending fluid is handled by an arbitrary Lagrangian-Eulerian method. The results indicate that the density contrast, as well as the rotational velocity difference, between the hydrogel ball and the suspending fluid, play a central role in the ball's deformation due to centrifugal forces. This approach contributes to a deeper understanding of brain injuries and may portend the development of preventive measures and improved treatment strategies.

DOI: 10.1103/PhysRevFluids.10.030502

## I. INTRODUCTION

Traumatic brain injury (TBI) is a common injury that occurs when the brain is damaged due to a sudden impact to the skull. Situations in which people can experience TBI are widespread, such as for military personnel, during athletics, or from accidents such as falls or automobile collisions. Each case can have minor to fatal outcomes for all age ranges. The Centers for Disease Control and

*These authors contributed equally to this work.
†Contact author: ptyue@vt.edu
‡Contact author: qianhong.wu@villanova.edu

    

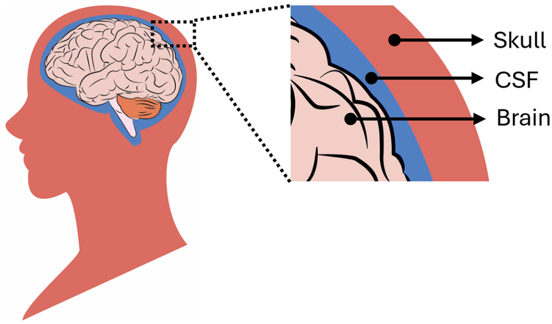


FIG. 1. The structure of a head.

Prevention (CDC) reported 214,110 TBI-related hospitalizations in 2020 and 69,473 TBI-related deaths in 2021 [1]. Overall, an estimated $40.6 billion was directed to nonfatal TBI treatment in 2016 alone, with an expected loss from all cases to be even greater [2].

The concern about TBI's prevalence has motivated a wide range of experimental and theoretical approaches in uncovering the behavior of the brain during impact. To observe TBI directly, animal testing can be performed for accuracy in biology and impact response [3,4]. These biological models are necessary for observing post-injury effects, but they are limited in observing impacts at the time of blow due to the opaque skull. Clinical studies have used advanced tools like MRI to examine the brain's condition after a concussion [5]. Yet, these studies also focus on what happens post-injury, often overlooking the critical moments during the impact itself. Physical models can be created to capture impact data by allowing transparency and sensors into the brain's otherwise isolated environment. These models can then be subject to consistent translational impact tests to capture impact data. Scientists have also used numerical studies and simulations to examine which part of the brain is injured [6]. The challenge is that numerical studies need experiments to validate their results.

Figure 1 shows the basic structure of the head, where the soft brain tissue is enclosed in the hard skull; between them, there is a thin subarachnoid space (SAS) which is filled with cerebrospinal fluid (CSF). Two types of impacts can affect the head: translational and rotational impacts. A translational impact results in rapid linear acceleration and deceleration of the brain within the skull. This relative motion can cause various types of brain injuries through different biomechanical processes, including coup and contrecoup injuries [7], shearing forces [8], intracranial pressure changes [9], and secondary injury processes [10]. A rotational impact on the head involves angular acceleration and deceleration of the brain within the skull, leading to shearing forces and diffuse axonal injury (DAI) [8], tissue strain [11], rotational cavitation [12], and secondary injury processes [10]. Rotational impacts are particularly harmful because the brain is less able to withstand angular acceleration than linear acceleration. The complex and interconnected nature of the brain's neural networks makes them especially vulnerable to rotational forces.

Despite extensive studies on the injury mechanisms of TBI, the way brain injuries transpire, mechanically and biologically, is still not fully understood. Intuitively, when an impact is imposed on the head, it will be transmitted from the hard skull through the viscous CSF to the soft brain matter. The presence of the CSF will also dampen the force and mitigate the impact on the brain. However, in current brain concussion research, the role of transient CSF flow in the SAS has long been overlooked. For example, finite element analysis (FEA) of brain injury [13], although it considers the detailed properties of the brain, often treats the CSF as part of the solid brain with certain viscoelastic properties. Consequently, it misses the key physics of the CSF during the brain concussion process. One of the few studies related to the CSF flow during a rotational impact process was performed by Lang *et al.* [14], who utilized an egg analog to investigate how rotational impacts are transmitted through a liquid medium to affect the soft matter within. A novel experimental study was developed where egg yolk bathed in a liquid environment and enclosed in a rigid container was exposed to rapid impacts. An intriguing observation was made, which shows that the egg yolk experienced the largest deformation during a rotational deceleration process. A simplified theoretical model was developed which shows that the fluid pressure outside the egg yolk was not large enough during the deceleration process to balance the centrifugal force. The study with egg yolk represents the first effort in demonstrating that decelerational impact is the primary factor influencing brain injury. However, the simplified theoretical model treats the egg yolk as a spherical ball of liquid surrounded by a massless membrane without deformations. While it outlines pressure variations outside the spherical ball during rotation, it lacks the complexity required for a true fluid-structure interaction model. As a result, it cannot accurately predict the real-time deformation of the egg yolk during impact events. A fundamental question arises: How can we precisely describe the highly transient fluid-structure interaction (FSI) between the CSF and the soft brain matter, and how can we relate this interaction to brain injury? Because rotational impacts are particularly harmful, we are especially interested in understanding the interaction between the CSF and the soft brain matter when the head is subjected to a sudden rotational impact.

To address this question, we are developing, in this paper, a comprehensive numerical and experimental study to create a fully validated theoretical framework. Although the brain is a complex, inhomogeneous biological system, our goal is to develop a high-fidelity numerical scheme that captures the key physics of the FSI between a soft matter and its liquid surroundings, both enclosed in a rigid container, when a rapid rotational impact is imposed on the container. To this end, we will use a simplified experimental setup where a homogeneous soft gel enclosed in a cylindrical container is exposed to sudden rotational impact. The motion and deformation of the soft matter will be recorded. Meanwhile, we will develop a numerical model based on the arbitrary Lagrangian-Eulerian (ALE) formulation, which will be compared and validated against experimental data. In this model, the soft gel that mimics the brain matter is treated as a poroelastic material while the surrounding liquid that mimics the CSF is treated as a Newtonian fluid. Once the theoretical framework is fully verified and validated, we aim to apply it to the prediction of brain injury in future studies.

## II. EXPERIMENTS

We mimic the brain with a hydrogel sphere that is suspended in a liquid bath that simulates the CSF. The sphere and the liquid are contained in a horizontal cylindrical container, and the rotational impact is realized by sudden changes in the rotational speed of the cylinder, as shown in Fig. 2.

In forming the hydrogel spheres, two spherical molds of 1.3 in and 1 in diameter are 3D printed out of photopolymer resin using an ELEGOO Saturn 2 MSLA 3D printer. The molds are used to shape a specialized PVA/BN (polyvinyl alcohol/boron nitride) gel for this experiment. The gel is formed by first dispersing BN (BN, powder, 1 μm, Sigma-Aldrich) in de-ionized water at room temperature, followed by sonication for 1 h. Then, PVA (Mw 146 000-186 000, 99% hydrolyzed, Sigma-Aldrich) is dissolved in the solution at a ratio of 3% PVA and 97% distilled water which is heated to 90 °C, and vigorously stirred for 5 h. After cooling down to room temperature, the solution is cast into the molds, frozen at −20 °C for 24 h, and then set to thaw for 12 h at room temperature (25 °C). Finally, the PVA/BN gel is broken out of the mold for further experimentation. This meticulous formation process is followed to ensure reproducibility in the physical properties of the gel sphere, especially its density and Young's modulus, and to fine-tune these properties to mimic the human brain. The density of the gel is calculated by measuring the volume of a sample in a graduated cylinder along with the mass on a scale. This determined the gel to have a density of 1.0456 g/ml, which is similar to real brain matter of 1.081 g/ml [15]. The Young's Modulus was determined to be between 0.2 and 1 kPa, within the range of real brain matter of 0.1 to 16 kPa [16–19].

Figure 2 displays the experimental setup of the cylinder and the contained gel ball to be rotated by the attached electric motor. To ensure the gel ball remains suspended and maintains a central

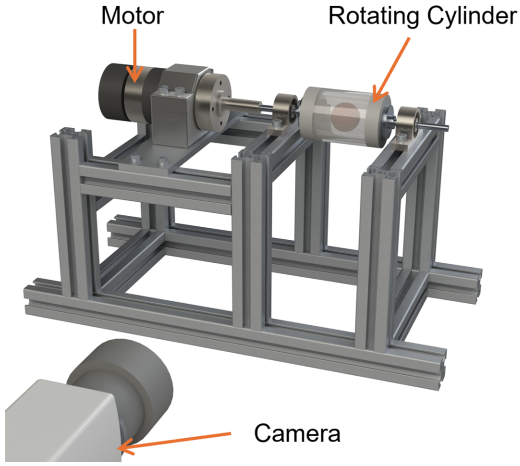


FIG. 2. Rotational experimental setup. The hydrogel ball is bathed in the rotating cylinder.

position during rotation, the surrounding fluid must have a higher density than the gel. Hence, an 80% glycerin solution of density 1.202 g/ml was used for this purpose [20]. The gel ball is encapsulated in the rigid transparent cylinder while fully submerged in the glycerin solution to eliminate air bubbles from being trapped inside. The sealed cylinder is then mounted with an electric motor on an 80/20 aluminum T-slot frame to increase rigidity. The motor is turned on, causing the cylinder to rotate. This motion, in turn, drives the fluid inside the cylinder to rotate, which then drags the soft gel ball suspended in the glycerin into rotation until it reaches a steady state. The motor is then turned off, causing the cylinder to stop rotating. Consequently, the soft gel ball experiences a deceleration process until it finally stops rotating as well. During this process, the rotation of the cylinder and the deformation of the hydrogel ball are captured by a Phantom® Miro® C110 high-speed camera at a frame rate of 1000 fps and a resolution of 1280 by 720 PPI. The velocity of the cylinder is calculated by tracking the rate of eight equally spaced markings on the cylinder wall passing the front view.

A representative experimental result is shown in Fig. 3. Figure 3(a) shows a snapshot of the cylinder and the gel ball during the rotation process, where the image of the hydrogel ball is characterized by its radial and axial dimensions, $\hat{a}$ and $\hat{b}$, respectively. To precisely capture the actual shape of the soft ball inside the cylinder, one must account for the refraction introduced by the liquid in the cylinder. According to Snell's law, the actual radial and axial dimensions of the gel ball can

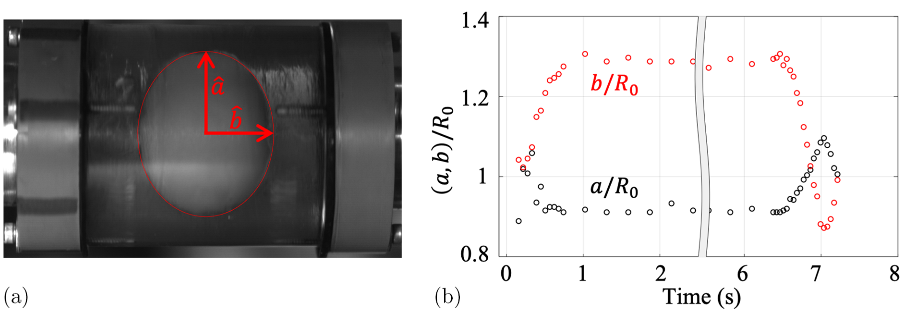


FIG. 3. (a) A snapshot of the cylinder and the gel ball whose shape is fitted with an ellipse with labeled radial dimension $\hat{a}$ and axial dimension $\hat{b}$. (b) Experimental data of ball deformation, characterized by the values of $a/R_0$ and $b/R_0$ over time, where $R_0$ is the initial radius of the hydrogel ball and $a = \hat{a}/n$, $b = \hat{b}$.

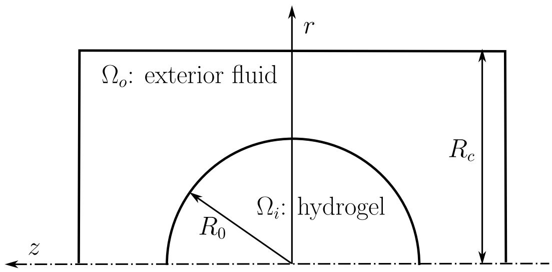


FIG. 4. A schematic of the computational domain.

be expressed as $a = \hat{a}/n$ and $b = \hat{b}$, where $n$ is the refractive index. The detailed derivation of the conversion can be found in Appendix A. The liquid used in this experiment is a mixture of 80% glycerol and 20% water with a refractive index of 1.428 based on our experimental measurements. Figure 3(b) depicts the experimental data where the cylinder is brought from a stationary state to a steady speed of 20 rev/s. Accompanying this acceleration process is the deformation of the gel ball, characterized by the values of $a$ and $b$ in the radial and axial directions, respectively. As shown in Fig. 3(b), the radial dimension of the ball $a$ shrinks by 8.2% while its axial dimension $b$ lengthens by 28.9%. This is maintained until the cylinder is set to stop at $t = 6.4$ s. The glycerin and the gel ball then experience a decelerating rotation process. Associated with this process is a sharp deformation of the gel ball, with $a$ being stretched and $b$ compressed, both overshooting their equilibrium values in a short period of 0.7 seconds. Finally, the ball reaches rest at $t = 7.3$ s where both deformation values equalize, representing a return to the ball's original spherical shape. An associated video of the experimental results shown in Fig. 3 can be found in Supplemental Material [21].

## III. COMPUTATIONAL METHODOLOGY

### A. Mathematical model

Deforming hydrogel in a suspending fluid constitutes a fluid-structure interaction problem. The computational domain, as shown in Fig. 4, comprises a hydrogel domain $\Omega_i$ and a clear fluid domain $\Omega_o$, partitioned by an interface $\Gamma$. The hydrogel can be conceptualized as a poroelastic medium composed of a solid structure along with an interstitial fluid.

Following [22], we have the following equations for hydrogel in $\Omega_i$:

$$\rho_f\left(\frac{\partial \mathbf{v}_f}{\partial t} + \mathbf{v}_f \cdot \nabla \mathbf{v}_f\right) = \nabla \cdot (\phi_f \boldsymbol{\sigma}_f) - \phi_f \nabla p + \mathcal{F}^{s\to f}, \tag{1}$$

$$\rho_s\left(\frac{\partial \mathbf{v}_s}{\partial t} + \mathbf{v}_s \cdot \nabla \mathbf{v}_s\right) = \nabla \cdot (\phi_s \boldsymbol{\sigma}_s) - \phi_s \nabla p + \mathcal{F}^{f\to s}, \tag{2}$$

$$\nabla \cdot (\phi_f \mathbf{v}_f + \phi_s \mathbf{v}_s) = 0, \tag{3}$$

$$\frac{\partial \phi_s}{\partial t} + \nabla \cdot (\phi_s \mathbf{v}_s) = 0, \tag{4}$$

$$\frac{d\mathbf{u}_s}{dt} = \mathbf{v}_s, \tag{5}$$

where $\rho_f$ and $\rho_s$ are the densities of the interstitial fluid and solid network, $\phi_f$ and $\phi_s$, satisfying $\phi_f + \phi_s = 1$, are the fluid and solid volume fractions, $\boldsymbol{\sigma}_f$ and $\boldsymbol{\sigma}_s$ are the fluid and solid stress tensors, $p$ is the pressure, and $\frac{d}{dt}$ denotes the material derivative. The Darcy drag between the solid skeleton and the solvent is defined as $\mathcal{F}^{s\to f} = -\mathcal{F}^{f\to s} = \xi \phi_f \phi_s (\mathbf{v}_s - \mathbf{v}_f)$. Equations (3) and (4) are the continuity equations of the hydrogel and its solid component, respectively. It should be noted that, although both the solid and fluid components are incompressible, the hydrogel may expand or shrink through the variation of volume fractions. The solid stress is a function of solid displacement $\mathbf{u}_s$, which is connected to the solid velocity $\mathbf{v}_s$ by the kinematic equation (5).

The clear fluid in $\Omega_o$ is governed by the incompressible Navier-Stokes equation:

$$\rho_o\left(\frac{\partial \mathbf{V}}{\partial t} + \mathbf{V}\cdot\nabla\mathbf{V}\right) = \nabla\cdot(\mathbf{\Sigma} - P\mathbf{I}), \tag{6}$$

$$\nabla\cdot\mathbf{V} = 0, \tag{7}$$

where $\rho_o$, $\mathbf{V}$, and $P$ are the density, velocity, and pressure of the clear fluid, respectively.

We assume both the the interstitial and clear fluids to be Newtonian and the viscous stresses are given by $\boldsymbol{\sigma}_f = \mu_e[\nabla\mathbf{v}_f + (\nabla\mathbf{v}_f)^{\mathrm{T}}]$ and $\mathbf{\Sigma} = \mu_o(\nabla\mathbf{V} + (\nabla\mathbf{V})^T)$, where $\mu_e$ is the effective viscosity of the interstitial fluid and $\mu_o$ is the viscosity of clear fluid. Regarding the solid stress, $\boldsymbol{\sigma}_s$, it is feasible to adopt hyperelastic models, as exhibited by Li *et al.* [22] However, for the sake of simplicity, we opt to use the following small-deformation linear elastic model in this context:

$$\boldsymbol{\sigma}_s = 2\mu_s\boldsymbol{\epsilon} + \lambda_s\mathrm{tr}(\boldsymbol{\epsilon})\mathbf{I}, \tag{8}$$

where $\mu_s$ and $\lambda_s$ represent the Lamé constants corresponding to the solid skeletal phase, whereas $\boldsymbol{\epsilon} = [\nabla\mathbf{u}_s + (\nabla\mathbf{u}_s)^{\mathrm{T}}]/2$ is the linear strain tensor.

On the gel-fluid boundary $\Gamma$, which moves with solid velocity $\mathbf{v}_s$, we impose the following boundary conditions:

$$\mathbf{n}\cdot(\mathbf{V} - \mathbf{v}_s) = \phi_f\mathbf{n}\cdot(\mathbf{v}_f - \mathbf{v}_s), \tag{9}$$

$$\mathbf{n}\cdot(\mathbf{\Sigma} - P\mathbf{I}) = \mathbf{n}\cdot(\phi_s\boldsymbol{\sigma}_s + \phi_f\boldsymbol{\sigma}_f - p\mathbf{I}), \tag{10}$$

$$(\mathbf{V} - \mathbf{v}_f)\cdot\mathbf{n} = \eta\,\mathbf{n}\cdot[(\mathbf{\Sigma} - P\mathbf{I}) - (\boldsymbol{\sigma}_s - p\mathbf{I})]\cdot\mathbf{n}, \tag{11}$$

$$(\mathbf{V} - \mathbf{v}_f)\cdot\mathbf{t} = \beta\,\mathbf{n}\cdot\mathbf{\Sigma}\cdot\mathbf{t}, \tag{12}$$

$$\phi_s(\mathbf{v}_s - \mathbf{v}_f)\cdot\mathbf{t} = -\beta\,\mathbf{n}\cdot\boldsymbol{\sigma}_s\cdot\mathbf{t}, \tag{13}$$

where $\mathbf{n}$ and $\mathbf{t}$ are the outward unit normal and tangent vectors to the hydrogel surface, and $\eta$ and $\beta$ are interfacial permeability and slip coefficients, respectively. Equations (9) and (10) denote mass balance and total traction balance, respectively. Equations (11)–(13), referred to as BC2 in [23], are designed such that the free energy of the isolated gel-fluid system does not increase in time [24,25]. The readers are referred to [23] for a detailed discussion of different boundary conditions between the hydrogel and the clear fluid.

### B. Numerical methods

The physical problem can be better described in the cylindrical frame with coordinates $(r, z, \theta)$. If we ignore the initial transient when the hydrogel ball is off-center, then the flow is axisymmetric, i.e., all functions are independent of the azimuthal coordinate $\theta$. Thus the three-dimensional problem reduces to a two-dimensional axisymmetry problem in the $(r, z)$ plane, as shown in Fig. 4. However, due to rotation, velocity and displacement can have nonzero $\theta$ components and thus we have to consider additional $\theta$ components for vectors (such as $\mathbf{v}_s$, $\mathbf{u}_s$, and $V$) and $r\theta$, $z\theta$, and $\theta\theta$ components for tensors (such as $\boldsymbol{\epsilon}$, $\boldsymbol{\sigma}_s$, and $\mathbf{\Sigma}$).

In our recent work [22], we formulated a finite-element algorithm to resolve the integrated motion and deformation of a gel-fluid system, where inertia is ignored. A C++ code was developed using the open-source finite-element library deal.II [26]. To simulate the rotational deformation of hydrogel in this work, we extend our previous formulation and code to include inertia and axisymmetry, with the weak form given in Appendix B. To track the motion of the gel-fluid interface as well as hydrogel deformation, we adopt a fixed-mesh ALE approach. Then the weak form (B1) and the mesh displacement equation are solved implicitly in a monolithic manner. P1 elements are used for pressures $p$ and $P$, and P2 elements are used for all other unknown functions. Time derivatives, which appear in the momentum equations [(1), (2), (6)] and the kinematic equation (5), are discretized using the first-order backward Euler method. Newton's method is used to solve the discretized nonlinear system that includes all the governing equations. More numerical details including mesh convergence tests can be found in [22].

In the following, we only focus on two numerical techniques specific to high-speed rotation. The governing equations (1)–(7), together with boundary conditions (9)–(13), guarantee energy dissipation, thus our mathematical problem is well posed. However, the high-speed rotation may cause numerical instabilities in the computation.

First, the hydrostatic pressure generated by the centrifugal force may obscure the pressure component that is responsible for fluid motion and hydrogel deformation in the $r$-$z$ plane. Both the solid and liquid components in our system are incompressible, and thus the pressures $p$ and $P$ are essentially Lagrange multipliers that enforce incompressibility. For a system with no stress boundary condition, a potential body force can be absorbed into the pressures without causing any flow or hydrogel deformation. We thus add a potential body force that counters the centrifugal force associated with the rigid-body rotation of the exterior fluid:

$$\mathbf{f} = -\nabla \Phi = -\rho_o r \bar{\omega}^2 \mathbf{e}_r, \tag{14}$$

where $\Phi = \frac{1}{2}\rho_o r^2 \bar{\omega}^2$ is the potential function, $\mathbf{e}_r$ is the unit vector in $r$ direction, and $\bar{\omega}$ is an angular velocity that characterizes the rotational flow. To be more specific, we add body forces $\mathbf{f}$, $\phi_f \mathbf{f}$, $\phi_s \mathbf{f}$ to the right-hand side of the momentum equations [(6), (1), (2)], respectively. It should be noted that the exact choice of $\bar{\omega}$ does not matter as long as the potential $\Phi$ can cancel out most of the pressure variation caused by centrifugal force. We find from numerical simulations that the average angular velocity of the exterior fluid is a good choice:

$$\bar{\omega} = \frac{\int_{\Omega_o} \frac{V_\theta}{r} d\Omega}{\int_{\Omega_o} d\Omega}. \tag{15}$$

Second, when the hydrogel undergoes rotation, the azimuthal displacement $u_{s,\theta}$, most of which comes from rigid-body rotation and does not trigger strain,[1] keeps increasing and leads to the so-called catastrophic cancellation (due to the subtraction of nearly equal numbers) in the evaluation of strain tensor. We therefore need to remove this contribution from rigid-body rotation such that the magnitude of $u_{s,\theta}$ is always at the same order as the other components of $\mathbf{u}_s$. To achieve this goal, we compute an instantaneous average angular displacement of the hydrogel

$$\alpha = \frac{\int_{\Omega_i} \frac{u_{s,\theta}}{r} d\Omega}{\int_{\Omega_i} d\Omega}, \tag{16}$$

and then reset $u_{s,\theta}$ to $u_{s,\theta} - r\alpha$. This operation is performed every few time steps before the magnitude of $u_{s,\theta}$ gets large.

## IV. RESULTS AND DISCUSSIONS

### A. Computational setup and parameter evaluation

Figure 4 shows the computational domain. A hydrogel ball, initially spherical with radius $R_0$, sits at the center of a cylinder with radius $R_c$ and half length $L_c$. The whole system is initially at rest and

[1]Consider a rigid-body rotation about the $z$ axis by an angle $\alpha$. The displacement is $\mathbf{u} = (\alpha \mathbf{e}_z) \times \mathbf{r} = \alpha x \mathbf{e}_y - \alpha y \mathbf{e}_x$, where $\mathbf{e}_x$, $\mathbf{e}_y$, and $\mathbf{e}_z$ are standard basis vectors and $\mathbf{r} = x\mathbf{e}_x + y\mathbf{e}_y + z\mathbf{e}_z$. It follows that $\nabla \mathbf{u} = \alpha(\mathbf{e}_y \otimes \mathbf{e}_x) - \alpha(\mathbf{e}_x \otimes \mathbf{e}_y)$ is an antisymmetric tensor, and $\nabla \mathbf{u} + \nabla \mathbf{u}^T = 0$, i.e., the strain is identically zero.

TABLE I. Computational parameters.

| parameters | values |
|---|---|
| solid density $\rho_s$ (Kg/m$^3$) | $1.0456 \times 10^3$ |
| solvent density $\rho_f$ (Kg/m$^3$) | $1.0456 \times 10^3$ |
| initial solid volume fraction $\phi_0$ | 0.03 |
| solvent viscosity $\mu_e$ (Pa s) | $10^{-3}$ |
| shear modulus $\mu_s$ (Pa) | $5.75 \times 10^3$ |
| Lamé's first parameter $\lambda_s$ (Pa) | $5.16 \times 10^4$ |
| Darcy drag coefficient $\xi$ (Pa s/m$^2$) | $2.5 \times 10^{10}$ |
| interfacial permeability $\eta$ (m/(Pa s)) | $4.24 \times 10^{-5}$ |
| interfacial slip coefficient $\beta$ (m/(Pa s)) | $4.24 \times 10^{-5}$ |
| exterior fluid density $\rho_o$ (Kg/m$^3$) | $1.202 \times 10^3$ |
| exterior fluid viscosity $\mu_o$(Pa s) | 0.06 |
| hydrogel initial radius $R_0$ (m) | $1.27 \times 10^{-2}$, $1.65 \times 10^{-2}$ |
| cylinder inner radius $R_c$ (m) | $1.905 \times 10^{-2}$ |
| cylinder half length $L_c$ (m) | $2.29 \times 10^{-2}$ |
| steady angular velocity $\omega_0$ (rad/s) | 94.88, 125.66, 152.68 |

then the cylinder starts to rotate with a constant acceleration until the angular velocity reaches $\omega_0$. The cylinder maintains steady rotation for a few seconds and then decelerates to a complete stop. The computational parameters, listed in Table I, are chosen based on experiments.

The effective viscosity of the solvent $\mu_e$ takes the value of water. The Lamé parameters $\mu_s$ and $\lambda_s$ correspond to a solid skeleton with Poisson's ratio $\nu = 0.45$ and effective Young's modulus $\phi_{s,0}E = 500$ Pa, where $E$ is the Young's modulus of the pure solid phase. The Darcy drag coefficient $\xi$ corresponds to the experimentally measured permeability $k = \frac{\mu_e(1-\phi_0)}{\xi\phi_0} = 1.3 \times 10^{-12}$ m$^2$. On the gel-fluid interface, there is no existing experimental measurement of interfacial permeability $\eta$ and slip coefficient $\beta$. The current choice corresponds to a penetration length $\frac{\eta}{\mu_e} = 4.24 \times 10^{-2}$ m and a slip length $\frac{\beta}{\mu_o} = 7.07 \times 10^{-4}$ m, which means the exterior fluid can freely penetrate into the hydrogel and the velocity slip between exterior fluid and the hydrogel is negligible.

### B. Comparison with experiments

Figure 5(a) shows the computed hydrogel deformation history together with experimental measurements. Here, we use two dimensionless parameters, namely $D_a = \frac{a-R_0}{R_0}$ and $D_b = \frac{b-R_0}{R_0}$, to quantify the deformation of hydrogel. Good agreement is achieved for the whole transient process and for different ball sizes and rotational velocities. For the small ball ($R_0 = 1.27 \times 10^{-2}$ m), Figs. 5(a) and 5(b) show essentially the same trend in deformation with the overshoot in deformation during the deceleration stage. This overshoot is however absent for the big ball ($R_0 = 1.65 \times 10^{-2}$ m), as shown in Fig. 5(c). This is probably due to the constraint of the cylinder walls.

For the steady-state deformation, we can get some qualitative results through a simple analysis. The effect of rotation can be reproduced by imposing a centrifugal force inside the hydrogel and a pressure load (caused by the centrifugal force in the exterior fluid) on the surface of the hydrogel. If we approximate the hydrogel as a linearly elastic solid and assume small deformation, then the elasticity problem becomes linear and the deviatoric strain is a function of Poisson's ratio $\nu$ and a dimensionless group $We = \frac{\Delta\rho(R_0\omega_0)^2}{\phi_0\mu_s}$ only. Here, $\Delta\rho = \rho_o - \rho_s$ is the density difference between the exterior fluid and the hydrogel. This parameter $We$, characterizing the ratio between inertia and elasticity, plays a similar role as the Weber number in drop dynamics. To be more specific, if $\nu$ is fixed, there exists the following relation for steady-state deformation:

$$D_b - D_a \propto We. \tag{17}$$

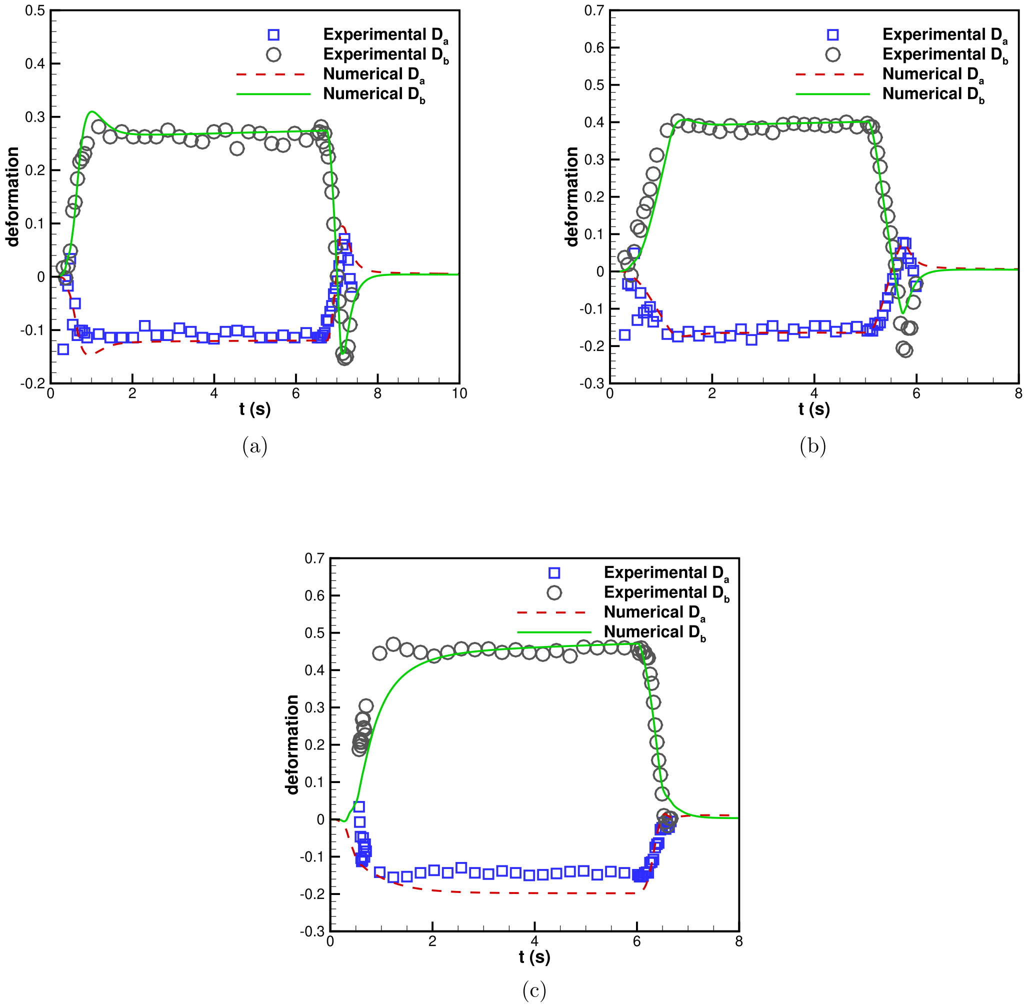


FIG. 5. Comparison of drop deformation history between computations and experiments. (a) $R_0 = 1.27 \times 10^{-2}$ m, $\omega_0 = 125.66$ rad/s, (b) $R_0 = 1.27 \times 10^{-2}$ m, $\omega_0 = 152.68$ rad/s, and (c) $R_0 = 1.65 \times 10^{-2}$ m, $\omega_0 = 94.88$ rad/s.

For the three test cases in Fig. 5, we have $We = 0.7967$, 1.1761, and 0.7675, respectively. The ratio of the first two is consistent with the steady-state deformations $D_b - D_a \approx 0.38$ and 0.45 in Figs. 5(a) and 5(b).

For transient behavior, simple analysis as above is no longer sufficient and we have to resort to numerical simulations based on our hydrogel FSI model. Besides, numerical simulations offer us detailed information on the flow field, which may help us better understand the physical process.

### C. Flow field

In this subsection, we will take the test case in Fig. 5(a) as an example and showcase the flow field during the transient process. In the beginning, we increment the cylinder's rotational velocity from 0 to 20 rev/s with a constant acceleration of 42.51 rev/s$^2$, and in the end, we slow down the cylinder's rotation with a constant acceleration of $-64.73$ rev/s$^2$. The whole process can be roughly

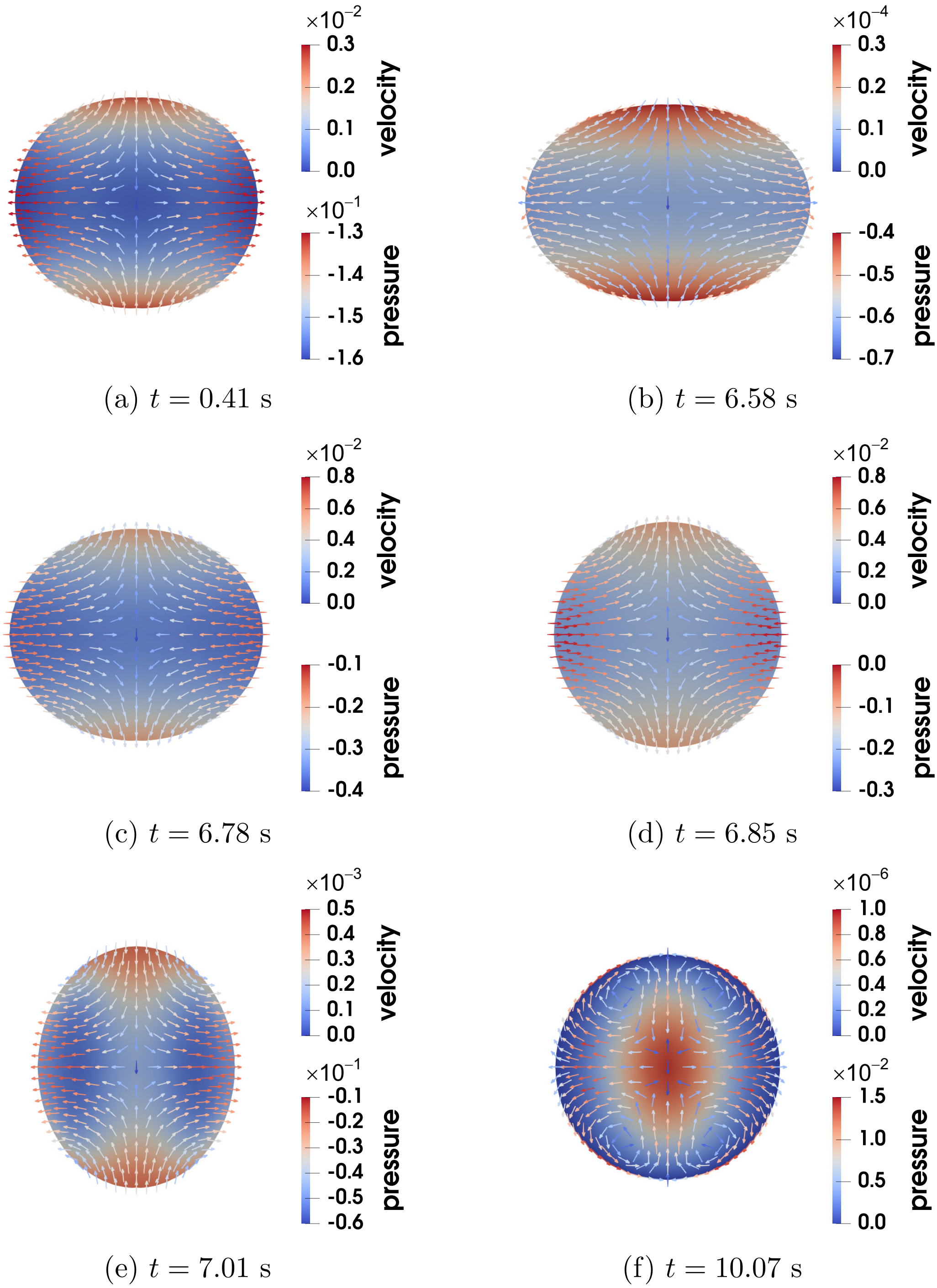


FIG. 6. Velocity and pressure inside the hydrogel ball. $R_0 = 1.27 \times 10^{-2}$ m, $\omega_0 = 125.66$ rad/s. The velocity value is dimensionless with the reference $v_{ref} = R_c\omega_0 = 2.88$ m/s. The pressure value, normalized by $p_{\text{ref}} = \mu_s = 2.49$ kPa, is relative to the average pressure on the cylinder wall.

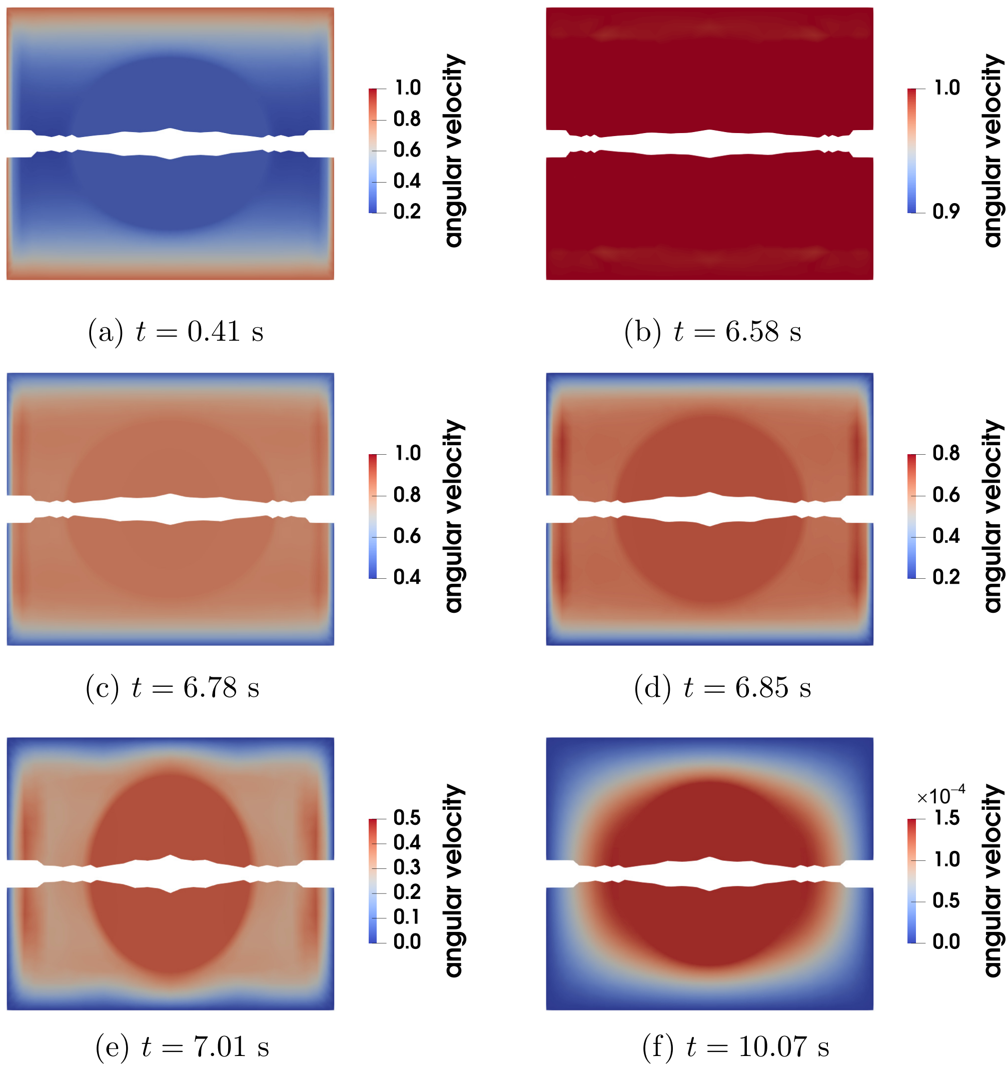


FIG. 7. Angular velocity of the hydrogel ball and the suspending fluid. The values are dimensionless with the reference $\omega_{ref} = \omega_o = 125.66$ rad/s. The layer of cells adjacent to the axis of symmetry, where the evaluation of angular velocity is inaccurate, is not shown.

divided into three distinct stages based on cylinder motion: acceleration (0 to 0.5 s), steady rotation (0.5 to 6.6 s), and deceleration (>6.6 s).

Equating the Darcy drag $\xi\phi_f\phi_s|\mathbf{v}_f - \mathbf{v}_s|$ with the centrifugal force $(\rho_o - \rho_s)r\omega^2$, we get a dimensionless group characterizing the ratio between interphase slip $|\mathbf{v}_f - \mathbf{v}_s|$ in the hydrogel and the rotational velocity $r\omega$: $\frac{|\mathbf{v}_f-\mathbf{v}_s|}{r\omega} = \frac{(\rho_o-\rho_s)\omega}{\xi\phi_f\phi_s} = 2.7 \times 10^{-6} \ll 1$. This means the relative motion between the solvent and the solid skeleton is vanishingly small. Our numerical computation confirms that $\frac{|\mathbf{v}_f-\mathbf{v}_s|}{R_c\omega_0}$ is typically of order $10^{-6} \sim 10^{-5}$. This has two consequences in our favor. First, the flow is insensitive to the interfacial permeability $\eta$, which lacks experimental data. Second, the continuity condition (9), which is derived for equal densities between the solvent and the exterior fluid, can be directly adopted for nonequal densities with reasonable accuracy because of negligible interfacial permeation.

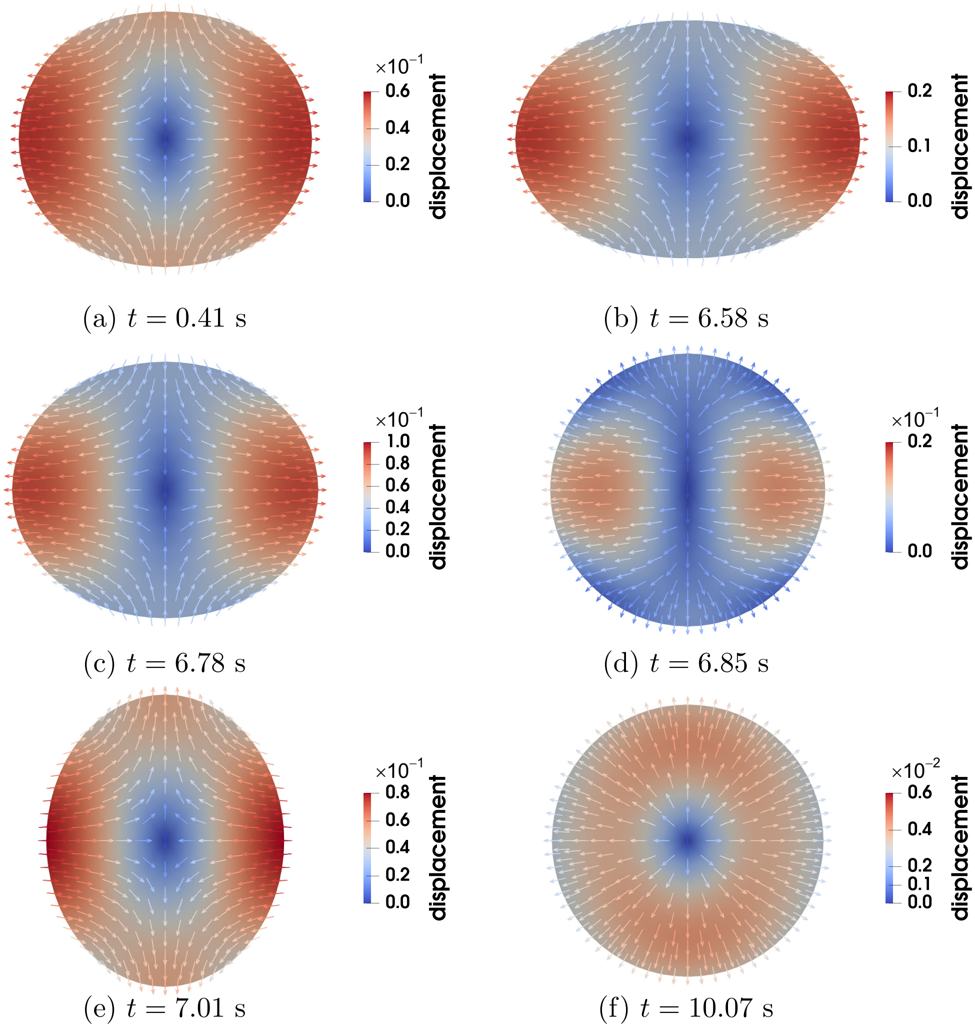


(a) $t = 0.41$ s (b) $t = 6.58$ s

(c) $t = 6.78$ s (d) $t = 6.85$ s

(e) $t = 7.01$ s (f) $t = 10.07$ s

FIG. 8. Solid displacement $\mathbf{u}$ in the hydrogel. The values are made dimensionless by the reference length $R_c$.

The snapshots of $\mathbf{v}_f$ (only components in the meridian $r$-$z$ plane) and $p$ inside the hydrogel and the angular velocity are given in Figs. 6 and 7. Figure 6(a) shows the typical flow field during cylinder acceleration—the hydrogel is being squeezed in the radial direction and stretched in the axial direction due to the centrifugal force of the exterior fluid. Due to inertia, the acceleration of hydrogel lags behind that of the exterior fluid, and consequently, the hydrogel has a lower angular velocity than the exterior, as shown in Fig. 7(a). At steady rotation, the hydrogel assumes a prolate spheroidal shape as shown in Fig. 6(b). Since $\mathbf{v}_s \approx \mathbf{v}_f$, the small magnitude of $\mathbf{v}_f$ indicates that the hydrogel is no longer deforming and the deformation has stabilized. Meanwhile, the hydrogel and the exterior fluid rotate with the same constant angular velocity $\omega_0$, i.e., the whole system is making a rigid-body rotation, as shown in Fig. 7(b).

The cylinder starts to decelerate at $t = 6.60$ s. Due to inertia, the deceleration of hydrogel lags behind that of the exterior fluid, and thus the hydrogel has a higher angular velocity as shown in Fig. 7(c). This causes the retraction of the hydrogel in the axial direction as indicated by the velocity vectors in Fig. 6(c). When the hydrogel returns to a shape close to its original spherical shape, as shown in Fig. 6(d), the magnitude of $\mathbf{v}_f$ peaks and the deformation continues. This causes a reversal

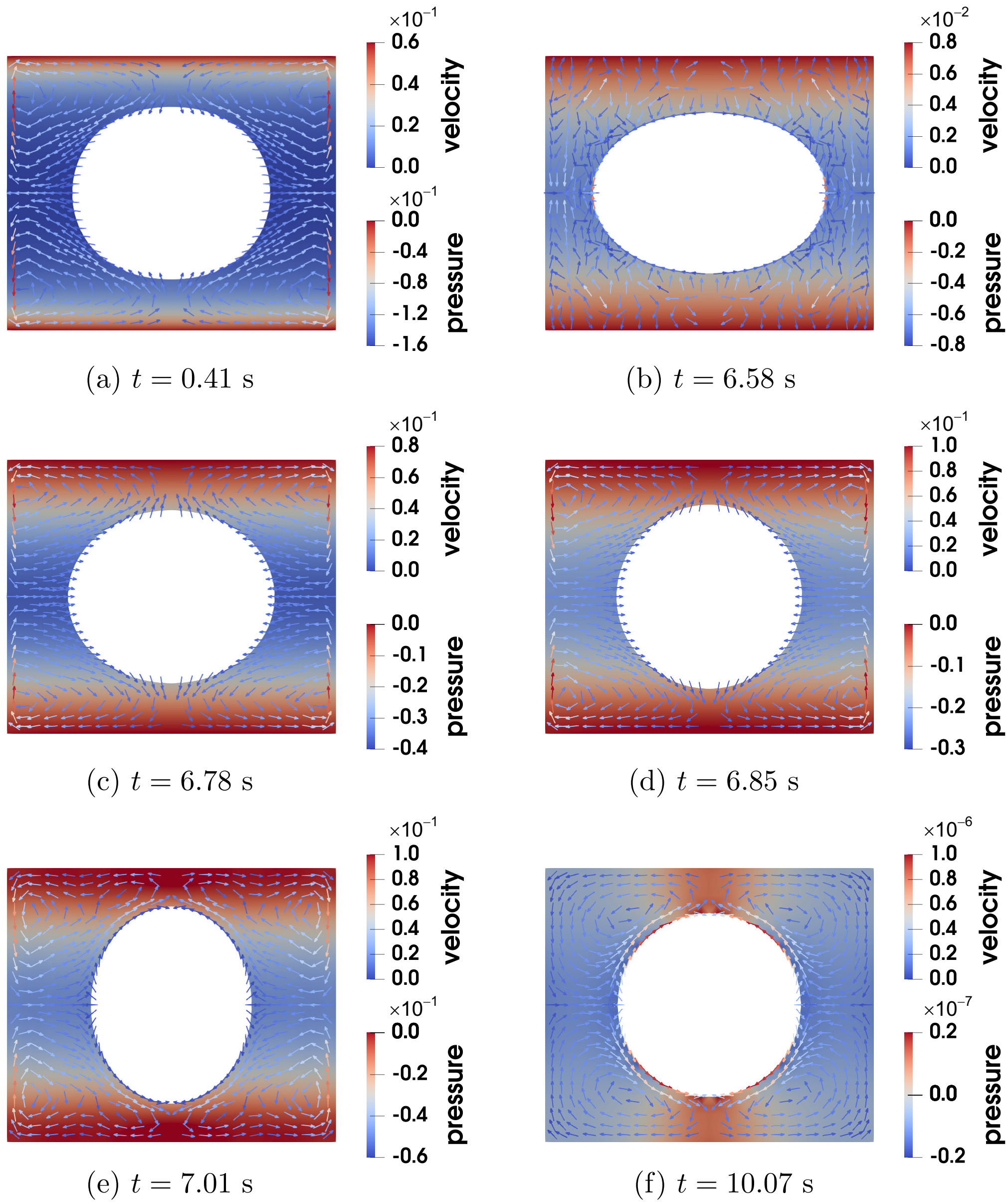


FIG. 9. Velocity **V** and pressure $P$ in the suspending fluid. The parameters are the same as Fig. 6.

of deformation and the hydrogel continues to evolve into an oblate spheroid as shown in Fig. 6(e). As the rotation dies down, the hydrogel eventually restores to its original shape as shown in Figs. 6(f) and 7(f).

For completeness, we also provide the solid displacement field inside the hydrogel in Fig. 8 and the flow field outside the hydrogel in Fig. 9. The displacement **u** behaves as expected from the shape of the hydrogel. The only thing worth noting is that the hydrogel remains slightly dilated when it stops rotating as shown in Fig. 8(f). This can be explained by the long time scale for the elastic stress to squeeze out the interstitial fluid. This time scale, denoted by $t_s$, can be estimated by balancing the elastic stress gradient $\frac{\mu_s}{R_0}$ with the Darcy drag $\xi v \sim \xi \frac{R_0}{t_s}$, which leads to $t_s \sim \frac{\xi R_0^2}{\mu_s} \approx 700\,\mathrm{s}$. Thus we expect the solid displacement to approach zero at a much later time.

When the liquid rotates [see Figs. 9(a)–9(e)], the pressure $P$ in the exterior fluid is dominated by the hydrostatic pressure due to the centrifugal force, as evidenced by the pressure gradient only in the radial direction. Since the outer fluid has no resistance from the Darcy drag, the flow velocity $\mathbf{V}$ in the $r$-$z$ plane appears to have greater magnitude than that inside the hydrogel (see Fig. 6). The velocity field in Fig. 9(b) appears irregular, which is a result of numerical error and visualization artifact. In this snapshot, the whole system is under steady rotation and the velocity magnitude in the $r$-$z$ plane approaches zero. However, the rotational velocity $V_\theta$ has a dimensionless value of order $O(1)$. This makes it difficult to accurately resolve the vanishing velocity components in the $r$-$z$ plane with numerical values of order $O(10^{-3})$.

## V. CONCLUSIONS

Traumatic brain injury inflicts a significant health and economic burden on society. To develop effective prevention and intervention strategies, it is critical to understand how the cerebrospinal fluid (CSF)-bathed brain responds to sudden external impacts. However, due to the brain's forbidding complexity, the small confines of the subarachnoid space (SAS), the extremely transient feature, and the skull's opacity preventing direct visualization of any complex physical interactions between the CSF flow and the compliant brain, the mechanism of brain concussion, especially the critical role of the transient CSF flow through the thin SAS during the concussion process, remains unclear.

In this paper, we have developed an experimental and theoretical approach to examine the fluid-structure interaction between a soft gel and its liquid surroundings, both enclosed in a rigid container, as a rapid rotational impact is imposed on the container. Our experimental results indicate that the gel ball experiences significant deformation during the decelerating rotational impact process. Our theoretical model, based on the arbitrary Lagrangian-Eulerian method, precisely captures this feature. More importantly, the numerical model is conclusively verified and validated against the experimental data. With a fully verified theoretical framework, this paper establishes a strong foundation for studying the highly transient fluid-structure interaction between soft matter, such as brain tissue, and the surrounding fluid, like CSF, when a sudden external impact is applied to the enclosing outer shell.

Our results suggest that decelerating rotational impact is a key factor in causing brain tissue injury. To mitigate such injuries, one effective approach is to reduce the severity of rotational impacts by extending the deceleration time, which can be achieved by adding cushioning materials to protective gear like helmets.

## ACKNOWLEDGMENTS

This research was supported by the National Science Foundation under Award No. 2322067 (Wu, Wang, and Bates). J.Z. acknowledges the financial support by the Guangdong Basic and Applied Basic Research Foundation under Award No. 2023A1515110861, the National Natural Science Foundation of China under Award No. 12401511, and the Interdisciplinary Intelligence Super Computer Center of Beijing Normal University at Zhuhai. J.J.F. acknowledges the financial support by the Natural Sciences and Engineering Research Council of Canada under Awards No. 2019-04162, No. 2024-03982, and No. 586462-23. P.Y. acknowledges the financial support by National Science Foundation under Awards No. 2012480 and No. 2309732.

## APPENDIX A: BALL SHAPE CONVERSION DUE TO REFRACTION OF LIQUID

Suppose the hydrogel ball is a spheroid with equatorial radius $a$ and polar radius $b$, and its polar axis aligns with the axis of the cylindrical container. In the high-speed camera footage, the image of

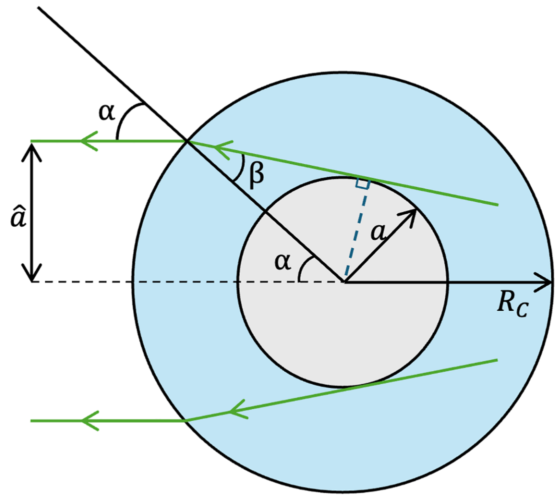


FIG. 10. Distortion of hydrogel ball image due to refraction.

the ball can be approximated as an ellipse with semi-axes $\hat{a}$ and $\hat{b}$, as shown in Fig. 3(a). Since the cylinder is straight in the horizontal direction, we have $\hat{b} = b$; but in the vertical direction we have $\hat{a} \neq a$ due to refraction, as shown in Fig. 10. According to Snell's law, the refracted angle $\alpha$ and the incident angle $\beta$ satisfy

$$\sin\alpha / \sin\beta = n, \tag{A1}$$

where $n$ is the refractive index of the fluid in the cylinder. From geometry, both $a$ and $\hat{a}$ are related to the radius of the cylinder $R_c$: $a = R_c \sin\beta$ and $\hat{a} = R_c \sin\alpha$. We therefore get the relationship between actual height $a$ and image height $\hat{a}$:

$$\hat{a}/a = n. \tag{A2}$$

This relation is exact as long as the ball is axisymmetric and centered in the cylinder and the thickness of the cylinder wall is negligible.

## APPENDIX B: FINITE-ELEMENT FORMULATION

In this Appendix, we provide a succinct summary of the weak form, in which inertia is taken into account. We define a weak solution of $\mathbf{V}$, $P$, $\mathbf{v}_f$, $\mathbf{v}_s$, $\mathbf{u}_s$, $p$, and $\phi_s$, and the corresponding test functions $\Psi_\mathbf{V}$, $\Psi_P$, $\Psi_{\mathbf{v}_f}$, $\Psi_{\mathbf{v}_s}$, $\Psi_{\mathbf{u}_s}$, $\Psi_p$, and $\Psi_{\phi_s}$, respectively. The weak form of Eqs. (1)–(3) and (6) and (7) can be obtained by taking the inner products of Eq. (1) with $\Psi_{\mathbf{v}_f}$, Eq. (2) with $\Psi_{\mathbf{v}_s}$, and Eq. (3) with $\Psi_p$ in $\Omega_i$, and Eq. (6) with $\Psi_\mathbf{V}$ and Eq. (7) with $\Psi_P$ in $\Omega_o$. Summing all these inner products and integrating by parts, we obtain the weak form for the governing equations:

$$\left(\rho_o\left(\frac{\partial \mathbf{V}}{\partial t} + \mathbf{V}\cdot\nabla\mathbf{V}\right), \Psi_V\right)_{\Omega_o} + (\boldsymbol{\Sigma}, \nabla\Psi_\mathbf{V})_{\Omega_o} - ((\boldsymbol{\Sigma} - P\mathbf{I})\cdot\mathbf{n}, \Psi_\mathbf{V})_{\partial\Omega_o}$$

$$- (P, \nabla\cdot\Psi_\mathbf{V})_{\Omega_o} + (\nabla\cdot\mathbf{V}, \Psi_P)_{\Omega_i} + \left(\rho_f\left(\frac{\partial \mathbf{v}_f}{\partial t} + \mathbf{v}_f\cdot\nabla\mathbf{v}_f\right), \Psi_{\mathbf{v}_f}\right)_{\Omega_i} + (\phi_f\boldsymbol{\sigma}_f, \nabla\Psi_{\mathbf{v}_f})_{\Omega_i}$$

$$- (\phi_f(\boldsymbol{\sigma}_f - p\mathbf{I})\cdot\mathbf{n}, \Psi_{\mathbf{v}_f})_{\partial\Omega_i} + \left(\rho_s\left(\frac{\partial \mathbf{v}_s}{\partial t} + \times v_s\cdot\nabla\mathbf{v}_s\right), \Psi_{\mathbf{v}_s}\right)_{\Omega_i} + (\phi_s\boldsymbol{\sigma}_s, \nabla\Psi_{\mathbf{v}_s})_{\Omega_i}$$

$$- (\phi_s(\boldsymbol{\sigma}_s - p\mathbf{I})\cdot\mathbf{n}, \Psi_{\mathbf{v}_s})_{\partial\Omega_i} - (p, \nabla\cdot(\phi_f\Psi_{\mathbf{v}_f} + \phi_s\Psi_{\mathbf{v}_s}))_{\Omega_i} + (\nabla\cdot(\phi_f\mathbf{v}_f + \phi_s\mathbf{v}_s), \Psi_p)_{\Omega_i}$$

$$+ (\xi\phi_f\phi_s(\mathbf{v}_f - \mathbf{v}_s), \Psi_{\mathbf{v}_f} - \Psi_{\mathbf{v}_s})_{\Omega_i}, + \left(\frac{1}{\eta}(\mathbf{V} - \mathbf{v}_f)\cdot\mathbf{n}, (\Psi_{\mathbf{V}} - \Psi_{\mathbf{v}_f})\cdot\mathbf{n}\right)_\Gamma$$

$$+ \left(\frac{1}{\beta}(\mathbf{V} - \mathbf{v}_f)\cdot\mathbf{t}, \Psi_{\mathbf{V}} - \Psi_{\mathbf{v}_f}\right)_\Gamma + \left(\frac{\phi_s^2}{\beta}(\mathbf{v}_s - \mathbf{v}_f)\cdot\mathbf{t}, \Psi_{\mathbf{v}_s} - \Psi_{\mathbf{v}_f}\right)_\Gamma = 0, \tag{B1}$$

where $\mathbf{n}$ is the unit normal vector pointing from the gel domain to the fluid domain and $(\cdot, \cdot)$ denotes the inner product over the region specified by the subscript. The weak forms of Eqs. (4) and (5) remain the same as in [22].

---


[1] Centers for Disease Control and Prevention, National center for health staticstics: Mortality data on CDC WONDER, https://wonder.cdc.gov/mcd.html, accessed: May 25, 2024.

[2] G. F. Miller, L. DePadilla, and L. Xu, Costs of nonfatal traumatic brain injury in the united states, 2016, Medical Care **59**, 451 (2021).

[3] X. Ma, A. Aravind, B. J. Pfister, N. Chandra, and J. Haorah, Animal models of traumatic brain injury and assessment of injury severity, Mol. Neurobiol. **56**, 5332 (2019).

[4] V. E. Johnson, D. F. Meaney, D. K. Cullen, and D. H. Smith, Animal models of traumatic brain injury, in *Traumatic Brain Injury, Part I*, Vol. 127 of Handbook of Clinical Neurology, edited by J. Grafman and A. M. Salazar (Elsevier, New York, 2015), Chap. 8, pp. 115–128.

[5] S. B. Shively, I. Horkayne-Szakaly, R. V. Jones, J. P. Kelly, R. C. Armstrong, and D. P. Perl, Characterisation of interface astroglial scarring in the human brain after blast exposure: a post-mortem case series, Lancet Neurol. **15**, 944 (2016).

[6] F. Hernandez, L. C. Wu, M. C. Yip, K. Laksari, A. R. Hoffman, J. R. Lopez, G. A. Grant, S. Kleiven, and D. B. Camarillo, Six degree-of-freedom measurements of human mild traumatic brain injury, Ann. Biomed. Eng. **43**, 1918 (2015).

[7] D. F. Meaney and D. H. Smith, Biomechanics of concussion, Clinics in Sports Medicine **30**, 19 (2011).

[8] V. E. Johnson, W. Stewart, and D. H. Smith, Axonal pathology in traumatic brain injury, Exp. Neurol. **246**, 35 (2013).

[9] R. M. Chesnut, N. Temkin, N. Carney, S. Dikmen, C. Rondina, W. Videtta, G. Petroni, S. Lujan, J. Pridgeon, J. Barber, J. Machamer, K. Chaddock, J. M. Celix, M. Cherner, and T. Hendrix, A trial of intracranial-pressure monitoring in traumatic brain injury, N. Engl. J. Med. **367**, 2471 (2012).

[10] D. J. Loane and A. Kumar, Microglia in the tbi brain: The good, the bad, and the dysregulated, Exp. Neurol. **275**, 316 (2016).

[11] T. A. Gennarelli and D. F. Meaney, Mechanisms of primary head injury, Neurol. Res. **17**, 115 (1995).

[12] L. Zhang, K. H. Yang, and A. I. King, A proposed injury threshold for mild traumatic brain injury, J. Biomech. Eng. **126**, 226 (2004).

[13] E. G. Takhounts, S. A. Ridella, V. Hasija, R. E. Tannous, J. Q. Campbell, D. Malone, K. Danelson, J. Stitzel, S. Rowson, and S. Duma, Investigation of traumatic brain injuries using the next generation of simulated injury monitor (simon) finite element head model, Stapp Car Crash Journal **2008**, 1 (2008).

[14] J. Lang, R. Nathan, and Q. Wu, How to deform an egg yolk? On the study of soft matter deformation in a liquid environment, Phys. Fluids **33**, 011903 (2021).

[15] T. W. Barber, J. A. Brockway, and L. S. Higgins, The density of tissues in and about the head, Acta Neurol. Scand. **46**, 85 (1970).

[16] W. Tyler, The mechanobiology of brain function, Nat. Rev. Neurosci. **13**, 867 (2012).

[17] T. Kaster, I. Sack, and A. Samani, Measurement of the hyperelastic properties of ex vivo brain tissue slices, J. Biomech. **44**, 1158 (2011).

[18] C. T. McKee, J. A. Last, P. Russell, and C. J. Murphy, Indentation versus tensile measurements of young's modulus for soft biological tissues, Tissue Eng. Part B **17**, 155 (2011).

[19] B. S. Elkin, E. U. Azeloglu, K. D. Costa, and B. Morrison, III, Mechanical heterogeneity of the rat hippocampus measured by atomic force microscope indentation, Journal of Neurotrauma **24**, 812 (2007).

[20] GP Association, *Physical Properties of Glycerine and Its Solutions*, Glycerine Producers' Association (Gulf Publishing Company, 1963), pp. 1–27.

[21] See Supplemental Material at http://link.aps.org/supplemental/10.1103/PhysRevFluids.10.030502 for description of visualization of rotational hydrogel ball.

[22] L. Li, J. Zhang, Z. Xu, Y.-N. Young, J. J. Feng, and P. Yue, An arbitrary Lagrangian-Eulerian method for simulating interfacial dynamics between a hydrogel and a fluid, J. Comput. Phys. **451**, 110851 (2022).

[23] Z. Xu, J. Zhang, Y.-N. Young, P. Yue, and J. J. Feng, Comparison of four boundary conditions for the fluid-hydrogel interface, Phys. Rev. Fluids **7**, 093301 (2022).

[24] Y.-N. Young, Y. Mori, and M. J. Miksis, Slightly deformable Darcy drop in linear flows, Phys. Rev. Fluids **4**, 063601 (2019).

[25] J. J. Feng and Y.-N. Young, Boundary conditions at a gel-fluid interface, Phys. Rev. Fluids **5**, 124304 (2020).

[26] D. Arndt, W. Bangerth, B. Blais, M. Fehling, R. Gassmöller, T. Heister, L. Heltai, U. Köcher, M. Kronbichler, M. Maier, P. Munch, J.-P. Pelteret, S. Proell, K. Simon, B. Turcksin, D. Wells, and J. Zhang, The deal.II library, Version 9.3, J. Num. Math. **29**, 171 (2021).